ACS Sustainable Chemistry & Engineering

pubs.acs.org/journal/ascecg

Research Article

# Black Phosphorus Quantum Dots/Carbon Nitride-Reduced Graphene Oxide Ternary Heterojunction as a Multifunctional Metal-Free Photocatalyst for Photooxidation Reactions

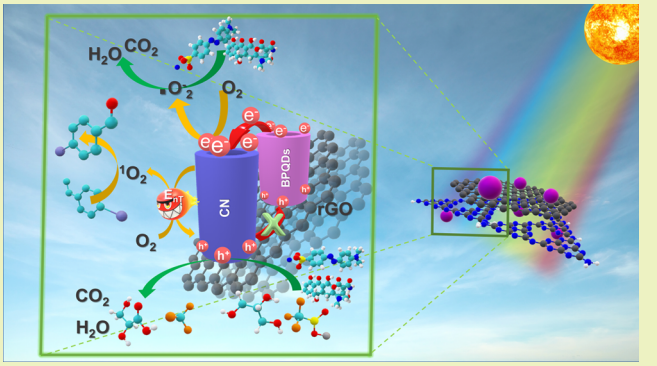
Zafer Eroglu, Melek Sermin Ozer, and Onder Metin*

Cite This: ACS Sustainable Chem. Eng. 2023, 11, 7560−7572

Read Online

ACCESS | Metrics & More | Article Recommendations | Supporting Information

**ABSTRACT:** We report herein a rationally designed metal-free ternary heterojunction, namely, black phosphorus quantum dots/carbon nitride-reduced graphene oxide (BPQDs/CN-rGO), that functions as a photocatalyst in multiple photooxidation reactions including C═C bond cleavage, glycerol oxidation, and C−$CF_3$ bond formation along with the removal of organic pollutants from wastewater. After the characterization of the structure and photophysical properties of BPQDs/CN-rGO heterojunction, it was first tested in the photodegradation of organic pollutants and showed superior performance. The underlying mechanism of BPQDs/CN-rGO in the photodegradation of organic pollutants revealed that the created internal electric field (IEF) among the components and photogenerated species ($h^+$ and $O_2^{\bullet-}$) are attributed to superior activity. Prompted by these results, the BPQDs/CN-rGO photocatalyst was applied in other photooxidation reactions. The nonclassical-type-II heterojunction structure generates active species ($O_2^{\bullet-}$, $h^+$, $^1O_2$) under visible light irradiation, enabling the selective oxidation of glycerol to glyceric acid and C═C bond cleavage along with highly challenging Langlois reagent to $CF_3$-functionalized heteroarenes.



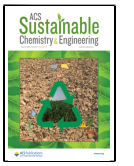

**KEYWORDS:** *black phosphorus quantum dots, photooxidation, heterojunction, photodegradation, trifluoromethylation*

## INTRODUCTION

Photocatalysis is an efficient tool that has received growing attention for a long time as a mean of converting solar energy into chemical energy.[1,2] Modern photocatalysis has verified its generality as being a versatile method for the progress of sustainability in academia and industry.[3−6] Semiconductor photocatalysts can be regarded to be at the core of photocatalysis due to their numerous capabilities for solar light absorption, electron−hole pair separation/migration, and surface catalytic redox reaction.[7,8] Hitherto, organic/inorganic semiconductors, heterojunction materials, semiconducting polymers, and so on have found widespread applicability owing to their unique properties (surface area, reusability, tuneability, etc.) along with green and eco-friendly nature.[9] Among them, heterojunction materials composed of two or more different semiconducting materials offer an opportunity to manipulate the photophysical properties of the selected materials for a targeted duty.[10−15] In addition, the construction of heterojunctions can complement the literature in terms of a multifunctional photocatalyst that can be designed with the aid of tuning band gap for many transformations.[16]

Zero-dimensional (0D) materials have emerged as key building blocks for constructing a variety of heterojunctions owing to their tunable redox band potentials.[10] Among them, black phosphorus quantum dots (BPQDs) have recently sparked a resurgence of attention owing to their distinctive structure consisting of an abundant element (P), high absorption co-efficiency with tunable band gap, quantum confinement effects, and easy hybridization with different materials.[17−20] Moreover, the facile surface functionalization of BPQDs with dissimilar materials or molecules improves their chemical stability toward oxygen and water while BPQDs contribute synergistically in terms of the layer-dependent tunable band gap.[21] For example, the coupling of BPQDs with reduced graphene oxide (rGO) provides a connection between the oxygen-containing functional groups and phosphorus atoms, thus improving their stability. Furthermore, rGO acts as an electron reservoir owing to its high conductivity, which enables the efficient flow of electrons from a semiconductor, resulting in an efficient electron−hole separation.[22] Therefore,

Received: February 21, 2023
Revised: April 12, 2023
Published: May 4, 2023



Downloaded via KOC UNIV on February 5, 2024 at 10:44:40 (UTC).
See https://pubs.acs.org/sharingguidelines for options on how to legitimately share published articles.

© 2023 The Authors. Published by American Chemical Society



https://doi.org/10.1021/acssuschemeng.3c01055
ACS Sustainable Chem. Eng. 2023, 11, 7560−7572

rGO is a promising candidate to couple with BPQDs at the interfaces for not only preventing fast recombination but also providing a large number of active sites as a consequence of its outstanding specific surface area.[23] However, the redox behavior of the BPQDs-rGO hybrid still requires an additional semiconductor for a selected transformation due to the conductivity of rGO. In this regard, carbon nitride (CN) as a third component might have a transformative impact on the BPQDs-rGO-based targeted heterojunction photocatalyst. There will be an effective contribution of CN to the binary heterojunction with regard to further stabilization and improvement of redox capacity due to strong $sp^2$-hybridized C and N bonds and a band gap of 2.7 eV, respectively.[11,24,25] As a result of establishing a heterojunction with these materials (BPQDs, rGO, and CN), a function-oriented photocatalyst can be constructed for both bond formation and bond cleavage in organic transformations. Such a cooperative photocatalyst system could be designed in a way to generate essential radical intermediates for building complex organic molecules while enabling indispensable reactive oxygen species (ROS) for the degradation of pollutants in water.[26,27] Considering the importance of these applications, the scope of a photocatalyst is a piece of valuable information to determine a point whether a substrate transforms into the desired compound.

For the purpose of designing a photocatalyst that operates in oxidative quenching reactions selectively, we present herein a ternary heterojunction consisting of earth-abundant elements, namely, BPQDs anchored on carbon nitride-reduced graphene oxide (CN-rGO) binary heterojunctions (denoted as BPQDs/CN-rGO hereafter). To find the best photocatalyst composition where the components synergistically formed a heterojunction with enhanced photocatalytic activity, the binary and ternary heterojunctions were prepared with different component ratios stepwisely. Each potential photocatalyst was tested on the photodegradation of methyl orange (MO) and tetracycline (TC) as organic pollutants. The superior photocatalytic performance of ternary heterojunction was obtained for the degradation of organic pollutions with high reaction kinetics. In contrast to the earlier reported catalyst,[28] the scope of the photocatalyst was extended to various photooxidative organic transformations such as C═C bond cleavage, glycerol oxidation, and C−$CF_3$ bond formation. By performing such experiments, the obtained redox ability by aligning Fermi levels based on internal electric field (IEF) was further proved.

## EXPERIMENTAL SECTION

**Synthesis of BPQDs.** Black phosphorus (BP) crystals were synthesized via low-pressure chemical vapor deposition[29] with slight modifications developed by our group.[30,31] By following the procedure in the literature for the synthesis of BP nanosheets (BPNSs), as-synthesized BP crystals (10 mg) were added into a 100 mL bottle with 50 mL of NMP and sonicated using probe sonication (5 °C, 200 W, 40% magnitude) for 1 h. After that, the resulting mixture was further exfoliated using an ultrasonic bath (5 °C, 215 W, 30−40 kHz) for 8 h. Next, the exfoliated BP was centrifuged at 3000 rpm for 30 min and 3/2 of the supernatant was taken and sonicated for 2 h with an ultrahomogenizer again to obtain BPQDs. The resulting BPQDs dispersion in NMP was directly used for the synthesis of ternary heterojunction photocatalyst (BPQDs/CN-rGO) or isolated via centrifugation at 12,000 rpm for 30 min and stored in an inert gas atmosphere for later characterization.

**Synthesis of CN and rGO.** CN was prepared via the thermal polycondensation method,[32] and rGO was synthesized according to the well-known modified Hummers method.[33,34]

**Preparation of Binary CN-rGO Heterojunction.** For the preparation of binary heterojunction with 3, 5, and 9 wt % rGO contents, as-prepared urea-based CN was taken in a certain amount (48.5, 47.5, and 45.5 mg, respectively) in 40 mL of EtOH in a glass bottle with a suitable cap and sonicated for 1 h in an ultrasonic bath (5 °C, 215 Watt, 30−40 kHz) in EtOH (7 mL). In parallel, a certain amount of rGO (1.5, 2.5, and 4.5 mg, respectively) was sonicated under the same conditions. Then, the dispersed rGO layers were added slowly within about 15 min into the resulting CN layers, and the resulting mixture was sonicated for an additional 3 h in order to provide a better interaction between the dispersed nanolayers in the solvent. Finally, centrifugation at 8500 rpm for 10 min was performed, and the resulting binary heterojunction was dried in a vacuum oven at 40 °C; it was stored for future use and analyses.

The resulting binary structures (3, 5, and 9 wt %) were named CN-$rGO_3$, CN-$rGO_5$, and CN-$rGO_9$ according to their rGO ratios, respectively.

**Preparation of Ternary BPQDs/CN-$rGO_3$ Heterojunction.** After the optimization of rGO content in the binary heterojunction concerning the result of MO degradation over the photocatalytic application, CN-$rGO_3$ was selected for the preparation of ternary heterojunctions. BPQDs/NMP solution with 10, 20, and 30 mL (vol %) ratios was added slowly to a well-dispersed binary heterojunction (45 mg of as-prepared CN-$rGO_3$ in 25 mL of NMP) in a glass bottle with a suitable cap and sonicated for 1 h in an ultrasonic bath (5 °C, 215 Watt, 30−40 kHz) separately. The resulting mixture was continued to sonicate for 3 h, centrifuged at 12,000 rpm for 30 min, and dried in a vacuum oven at 40 °C, resulting in the formation of desired ternary heterojunctions (Figure S1).

The ternary heterostructures with BPQDs ratios (10, 20, and 30 mL vol %) were named $BPQDs_1$/CN-$rGO_3$, $BPQDs_2$/CN-$rGO_3$, and $BPQDs_3$/CN-$rGO_3$, respectively.

## RESULTS AND DISCUSSION

**Structural and Photophysical Characterization of BPQDs/CN-rGO.** The schematic representation of the design for the targeted heterojunction is illustrated in Figure S3. Pristine CN and rGO were prepared by using the established procedures developed by our research group,[33−35] and they were combined at different ratios using the ultrasound-assisted liquid-phase exfoliation (UALE) method[28] to yield CN-rGO binary heterojunction. After selecting the best synergistically formed CN-rGO binary structure depending on their photodegradation efficiency, BPQDs were synthesized by using a top-down approach.[36] To screen the loading effect of BPQDs along with the purpose of improving their photocatalytic activity, they were anchored at different ratios on the corresponding CN-rGO binary heterojunction. To construct the targeted ternary heterojunction, denoted as BPQDs/CN-rGO, the UALE method[28] was used, and the characterization of the yielded ternary heterojunction and its precursors was started with X-ray diffraction (XRD). The determined crystal structures are depicted in Figure S4. The decrease in the intensity of the diffraction peak at $2\theta$ = 13.1° is attributed to the (100) diffraction plane of CN, which is the in-plane stacking of the planar tri-*s*-triazine. The major peak at $2\theta$ = 27.0° can be readily indexed to the (002) crystal plane of CN, corresponding to the interlayer stacking of conjugated aromatic rings. The broad peak of the (002) plane observed at $2\theta$ = 24.5° reveals the amorphous structure of synthesized rGO, while the relatively weak peak observed at $2\theta$ = 43.0° corresponds to the (100) diffraction plane of the hexagonal structure of carbon. The XRD pattern of binary and ternary heterojunctions consisted of CN and rGO patterns without any alteration, whereas the pattern of BPQDs was not clearly observed due to their low content compared to other



https://doi.org/10.1021/acssuschemeng.3c01055
ACS Sustainable Chem. Eng. 2023, 11, 7560−7572

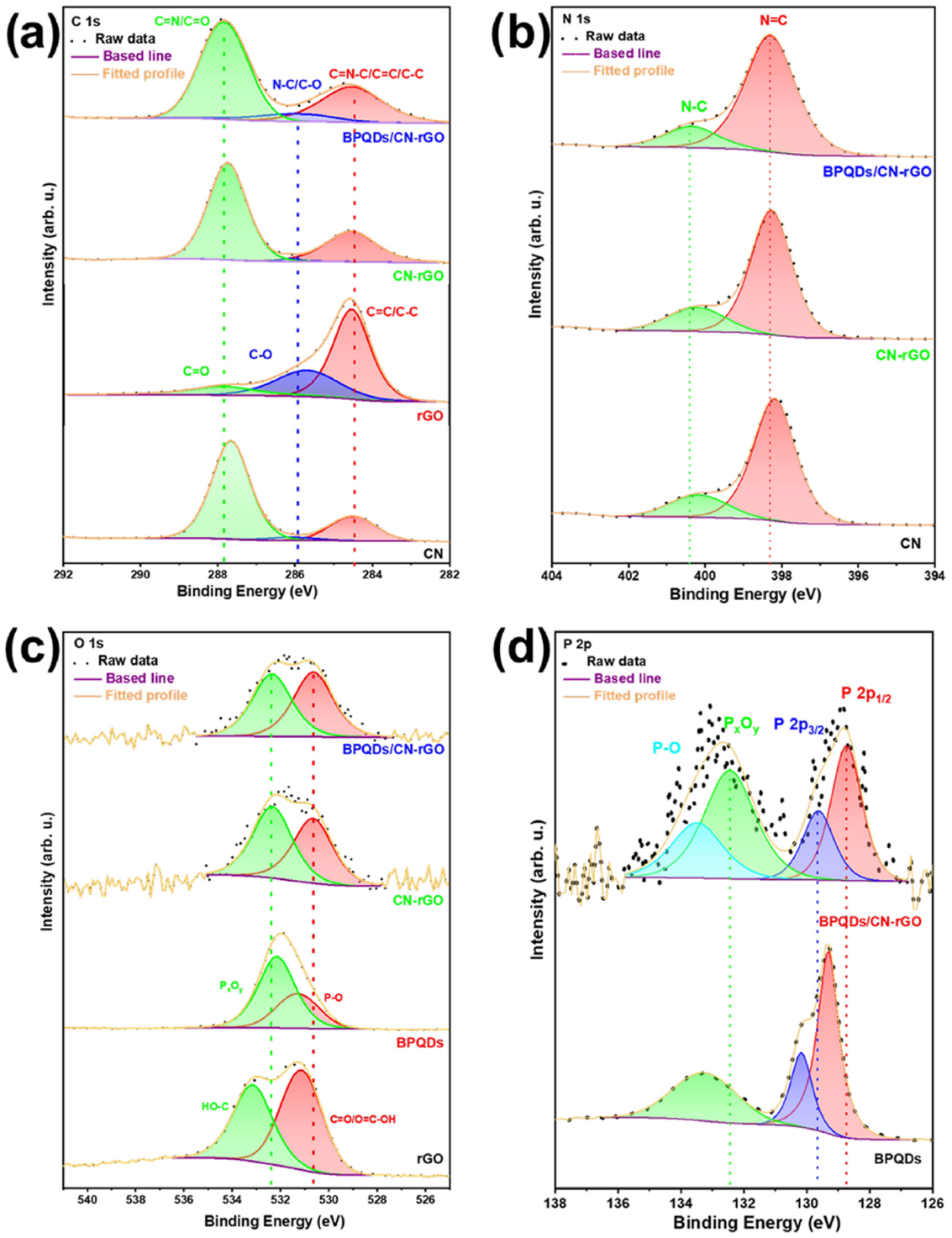



**Figure 1.** (a) High-resolution C 1s XPS spectra of CN, rGO, CN-rGO, and BPQDs/CN-rGO. (b) High-resolution N 1s XPS spectra of CN, CN-rGO, and BPQDs/CN-rGO. (c) High-resolution O 1s XPS spectra of rGO, BPQDs, CN-rGO, and BPQDs/CN-rGO. (d) High-resolution P 2p XPS spectra of BPQDs and BPQDs/CN-rGO.

nanomaterials. The shift of the peaks in the CN pattern indicates the interactions occuring between the components and formation of binary and ternary heterojunctions. The surface chemical compositions and chemical environment of each material were studied by X-ray photoelectron spectroscopy (XPS), as shown in Figure S5. The survey XPS spectra confirmed the successful deposition of as-prepared BPQDs on the CN-rGO binary heterojunction. The high-resolution XPS spectra of the C 1s region for CN, rGO, CN-rGO, and BPQDs/CN-rGO structures are given in Figure 1a. The expected three peaks of rGO at binding energies of 284.5, 285.7, and 287.9 eV were attributed to the C−C/C═C bonds, the oxygen-containing C−O, and C═O functional groups, respectively. The two main peaks of CN in the C 1s region are assigned to $C(N)_3$ at 284.5 eV and C═N at 287.6 eV in the tri-*s*-triazine aromatic ring as expected.[30] A slight shift was



https://doi.org/10.1021/acssuschemeng.3c01055
ACS Sustainable Chem. Eng. 2023, 11, 7560−7572

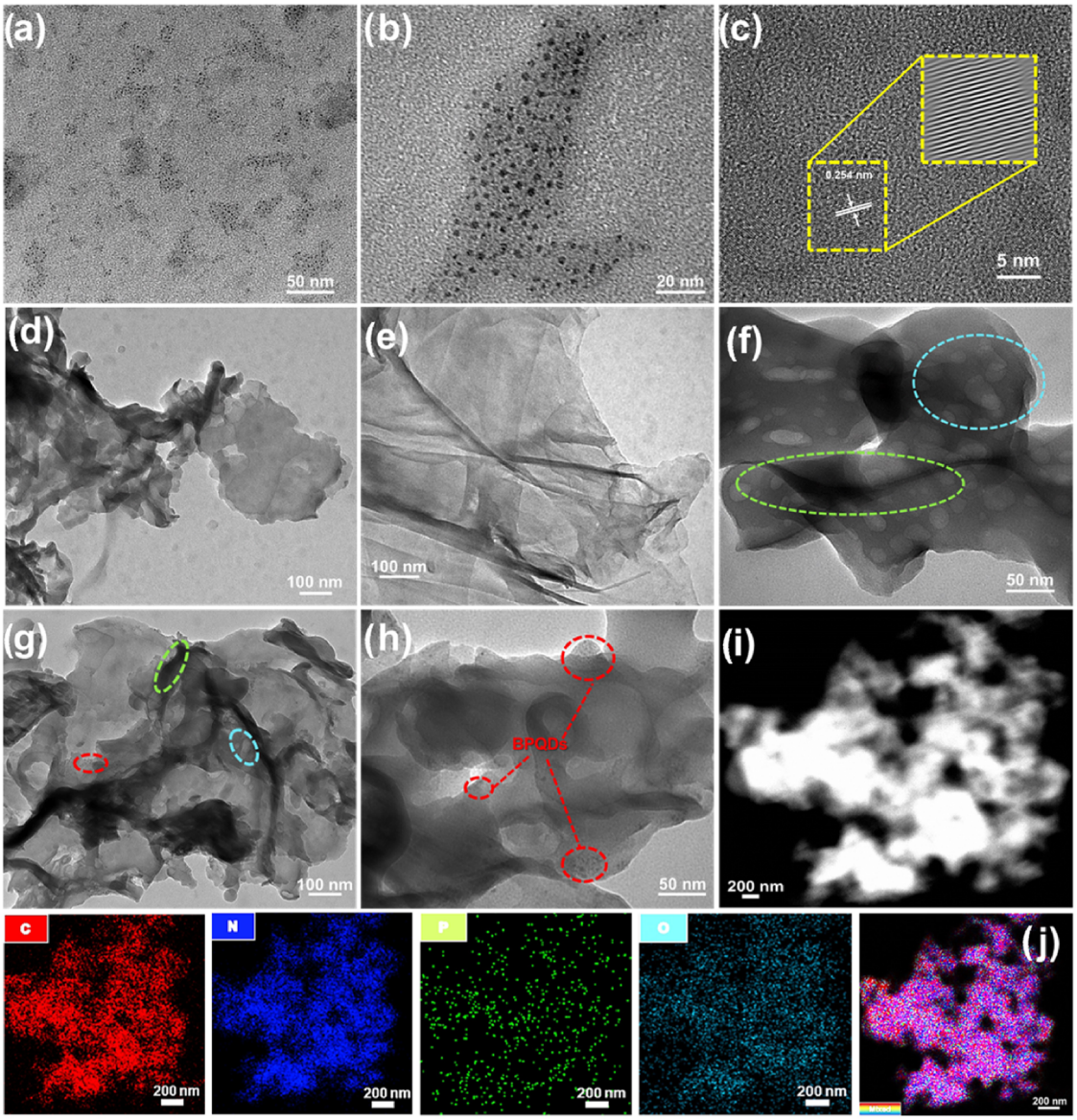



**Figure 2.** TEM images of (a, b) BPQDs. HR-TEM image of (c) BPQDs. TEM images of (d) CN, (e) rGO, (f) CN-rGO, and (g, h) BPQDs/CN-rGO. (i) HAADF-STEM image of BPQDs/CN-rGO. (j) HAADF-STEM-associated elemental mapping images of BPQDs/CN-rGO.

observed for the main peaks of binary CN-rGO structure while they were found to preserve their binding energy positions in the case of the BPQDs/CN-rGO ternary heterojunction compared to those of pristine materials. The high-resolution XPS spectra of the N 1s region of CN, CN-rGO, and BPQDs/CN-rGO are depicted in Figure 1b. The two main peaks located at binding energies of 398.1 and 400.2 eV were attributed to N atoms of C═N and $C(N)_3$−N in CN, respectively, displaying a slight shift toward higher binding energy compared to pristine CN. The high-resolution XPS spectra of the O 1s region exhibited two major peaks at binding energies of 531.2 and 533.2 eV, assigned to the C═O and C−O bonds of rGO, respectively, while two peaks were observed at binding energies of 531.3 and 532.2 eV and were attributed to the O atoms in P−O bonds and the $P_xO_y$ species of BPQDs, respectively[30] (Figure 1c). A slight shift of C 1s peak to the higher binding energy and lower binding energies of rGO in the O 1s atom region indicates that there is a strong interaction between these materials.[37] The high-resolution XPS spectrum of the P 2p region for BPQDs shows two main peaks with binding energies at 129.3 and 130.2 eV, corresponding to P $2p_{1/2}$ and P $2p_{3/2}$ core levels, respectively, implying that the oxidation state of phosphorus atoms remains unchanged as BP (Figure 1d).[31] In addition, the peak detected at a binding energy of 133.3 eV is ascribed to the $P_xO_y$ species due to the inevitable oxidation of BP during the sample preparation. The peaks of the P atoms in the ternary heterojunction, BPQDs/CN-rGO, are located at the lower energy binding energies compared to BPQDs. This apparent shift gave the first clue that electron flow from the CN-rGO binary heterojunction to BPQDs was established in the BPQDs/CN-rGO heterojunction. In addition, a new peak appeared at 132.4 eV due to P−N/P−O formation in BPQDs/CN-rGO, and the peak at 133.5 eV was assigned to oxidized P ($P_xO_y$) species.[30] This peak may also result from the interaction between the oxygen-containing functional groups of rGO/CN and the P atoms of BPQDs.[28,38]



https://doi.org/10.1021/acssuschemeng.3c01055
ACS Sustainable Chem. Eng. 2023, 11, 7560−7572

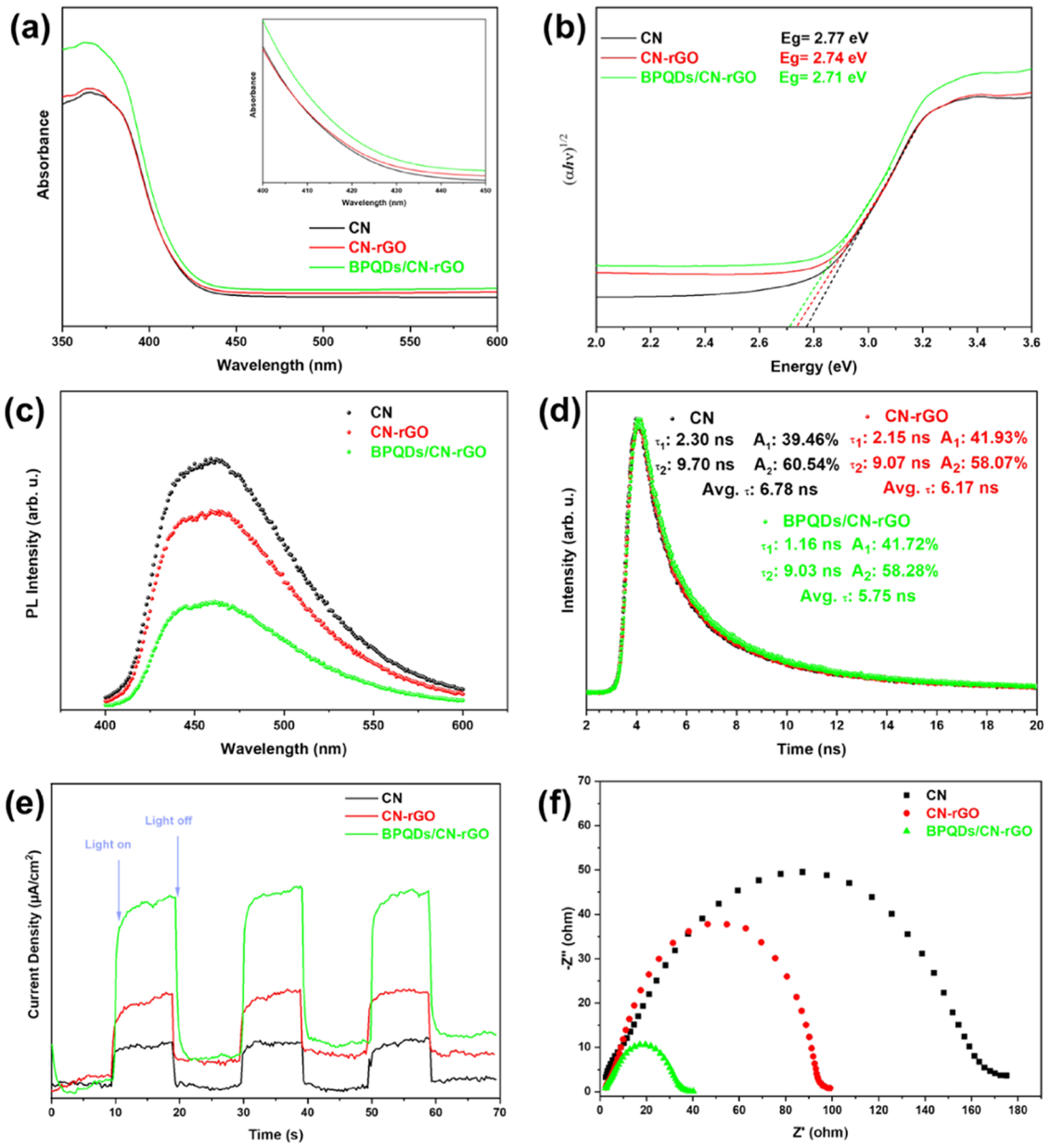



**Figure 3.** (a) Absorbance spectra (the inset shows enlarged absorbance spectra). (b) Tauc Plots. (c) PL spectra and (d) TRPL spectra. (e) Transient photocurrents spectra. (f) EIS spectra of CN, CN-rGO, and BPQDs/CN-rGO.

To gain further insights into the functional groups and the observed peaks attributed to the P−X (X: O, N) interactions in BPQDs/CN-rGO ternary heterojunctions, Fourier-transform infrared (FTIR) analysis was performed (Figure S6). Pristine CN exhibits characteristic peaks at 810 $cm^{-1}$ belonging to aromatic ring units in tri-*s*-triazine, while the vibrational modes in the 1100−1680 $cm^{-1}$ regions were described as the C−N and C═N bonds in these aromatic rings.[30] The characteristic peaks of functional groups attached to the edges of the CN were observed at 2160 $cm^{-1}$ and 3000 to 3600 $cm^{-1}$ ascribed to C≡N and N−H/$NH_2$ in the FTIR spectrum, respectively. The expected peaks for the functional groups in CN as well as the oxygen-containing −COOH and −OH stretching peaks in rGO were observed in the binary heterojunction at 1700 and ∼3300 $cm^{-1}$, respectively. All of the peaks defined for CN and rGO were also detected in the BPQDs/CN-rGO ternary heterojunction structure along with the P−N (887 $cm^{-1}$) and P−O (1082 $cm^{-1}$) stretchings as a result of the interaction of CN and rGO with BPQDs.[39] Raman spectra of BPQDs and BPQDs/CN-rGO structures are demonstrated in Figure S7. The three main peaks of BPQDs were attributed to the out-of-plane phonon mode ($A_g^1$) at 361.2 $cm^{-1}$ and two in-plane modes, $B_{2g}$ and $A_g^2$, at 436.9 and 464.5 $cm^{-1}$, respectively (Figure S7a).[21] However, these peaks screened in the range of 350−500 $cm^{-1}$ were not observed due to the low content of BPQDs in the ternary heterojunction. In Figure S7b, the two most intense peaks of rGO were detected at 1345.6 $cm^{-1}$ as the D band and the G band at 1585.5 $cm^{-1}$.[40] When Raman spectra of CN-rGO and BPQDs/CN-rGO were examined, it was observed that the intensities of the D and G bands of rGO remained unchanged. In addition, the blue shift of these rGO peaks in the CN-rGO and BPQDs/CN-rGO heterojunctions indicates that there are internal interactions between the components.


https://doi.org/10.1021/acssuschemeng.3c01055
ACS Sustainable Chem. Eng. 2023, 11, 7560−7572

Figure 2 shows transmission electron microscopy (TEM) images of CN, rGO, CN-rGO, and BPQDs/CN-rGO and high-angle annular dark-field scanning TEM (HAADF-STEM)-associated elemental mapping images of BPQDs/CN-rGO. The expected spherical 0D BPQDs with an average particle size of 2.5 nm were confirmed by the TEM images recorded at different magnifications as given in Figure 2a,b. In addition to that, a lattice fringe of 0.254 nm calculated from the high-resolution TEM image of a single BPQD clearly indicates the (111) plane of orthorhombic crystal structure, which is consistent with the previous reports (Figure 2c).[41] The mesoporous and nanolayered morphology of CN (Figure 2d) and the expected very thin, layered, and sheetlike structure of rGO (Figure 2e) were detected from the TEM images. The binary CN-rGO heterojunction was found to form a few-layered material where conductor rGO was located at the mesoporous CN (Figure 2f). Figure 2g,h demonstrates the homogeneous distribution of BPQDs in the binary CN-rGO heterojunction. HAADF-STEM and associated elemental mapping images of the BPQDs/CN-rGO heterojunction were examined to confirm the elemental composition (Figure 2i,j). These images clearly showed that the C, N, O, and P atoms are evenly distributed on the surface of the ternary heterojunction.

Ultraviolet−visible−near-infrared diffuse reflectance spectroscopy (UV−vis−NIR DRS) absorbance analysis was performed to examine the optical absorption capacities of the prepared CN, CN-rGO, and BPQDs/CN-rGO structures, shown in Figure 3a. Binary and ternary heterojunctions exhibit a slight increase in light absorption, particularly in the ultraviolet−visible (UV−vis) region compared to CN. In addition, CN-rGO and BPQDs/CN-rGO were found to have absorption bands approximately at 452 and 458 nm, respectively, which indicates the interaction-induced shift of the absorption threshold at the molecular level. This effect can be explained by the high light-harvesting feature of both rGO and BPQDs increasing the light-absorption ability of CN gradually after the decoration of these structures.[28] In Figure 3b, the Tauc plots of these structures were examined by using the Kubelka−Munk function, and the optical band gaps ($E_g$) of the structures were calculated.[42,43] The $E_g$ value of CN (2.77 eV) slightly decreased to 2.75 eV with the addition of rGO and then to 2.71 eV after the ternary heterojunction structure was formed with BPQDs and rGO. PL measurement is a beneficial method to investigate the dynamics of photogenerated charge carriers at the interface between the heterojunction components.[44] As shown in Figure 3c, the emission peak of pristine CN is observed at 448 nm due to the $n-\pi^*$ electronic transition, while fluorescence quenching was observed with the addition of rGO, attracting photogenerated charge carriers toward itself, as expected. The emission intensity was further decreased after the combination of BPQDs with the binary CN-rGO structure. The targeted decline in photogenerated $e^-/h^+$ recombination is greatly achieved for the constructed ternary heterojunction. At that point, the kinetics of the charge carriers for CN, CN-rGO, and BPQDs/CN-rGO were examined by the time-resolved PL (TRPL) method (Figure 3d). Both short- and long-lifetime values of CN-rGO and BPQDs/CN-rGO appeared to be enhanced compared to pristine CN. While the average lifetime for CN was 6.78 ns, this value decreased to 6.17 and 5.75 ns for CN-rGO and BPQDs/CN-rGO, respectively. Transient photocurrent and electrochemical impedance spectrum (EIS) were investigated for the photoelectrochemical characteristics of the materials. In Figure 3e, a weak response of CN and CN-rGO and a significant increase in the photocurrent of BPQDs/CN-rGO were observed. In this context, it can be said that the ternary heterojunction with a larger photocurrent response led to higher charge separation efficiency compared to the components.[45] The EIS spectrum in Figure 3f shows that the Nyquist curve does not start at zero because there is a certain solution resistance (about 2.5 Ω) during measurement. In the photocatalytic process with illumination, the impedance arc of CN-rGO is smaller than that of CN. The impedance arc of BPQDs/CN-rGO is smaller than that of CN-rGO, implying that the addition of BPQDs to CN-rGO can effectively reduce the conduction resistance of surface electrons.[45] The acceleration of all of these findings, the fast separation, and the migration of photogenerated charge carriers within ternary heterojunction show that the photophysical properties of the components are enriched.

**Photodegradation of Organic Pollutants.** For the utilization of solar energy, the desired ternary heterojunction was built stepwise to generate an ideal photocatalytic activity with the best synergistic effect between materials. The binary and ternary heterojunctions with different loadings were prepared, and their content in the heterojunction structures was associated based on their photocatalytic degradation efficiencies. Many strategies have been addressed to construct the electrostatic interaction between the oxygen-containing functional groups of rGO and the amine groups of CN efficiently, leading to strong $\pi-\pi$ stacking. As a result of these types of interactions, high electron migration and transfer occur at the interfaces of the nanomaterials.[28] First, binary CN-rGO heterojunctions with different rGO ratios (3, 5, and 9%) were prepared via the UALE method, and the yielded structures were named CN-$rGO_3$, CN-$rGO_5$, and CN-$rGO_9$, respectively. The synergistic effect of these obtained binary heterojunctions with different rGO contents was tested on the photodegradation of MO as a model reaction (Figure S10a). The photodegradation efficiency was examined at 5.0 ppm MO concentration with 30 mg photocatalyst amount for 30 min at 25 °C. During the reaction, the UV−vis absorbance values were measured at regular intervals, and the related absorbance values were converted to concentration. When the reaction was carried out under the catalyst-free medium and illumination, no change in MO concentration was observed (Figure S9a).

After optimization of the adsorption−desorption equilibrium at 30 min (Figure S8), the degradation efficiencies were calculated for each binary photocatalyst with different contents separately and summarized in Figure S9a. The pristine CN resulted in 42% degradation efficiency, while CN-$rGO_3$, CN-$rGO_5$, and CN-$rGO_9$ yielded 67, 51, and 48%, respectively. Despite the enhanced photocatalytic activity of the CN-rGO binary heterostructure compared to its pristine components, there is still room for improvement of their visible light-harvesting ability. In this regard, BPQDs as a 0D semiconductor nanomaterial were anchored on the binary CN-rGO heterojunction (Figure S3). After the binary heterostructure with the best rGO ratio was determined as CN-$rGO_3$, the corresponding binary heterojunction was loaded with different BPQD ratios (10, 20, and 30%) and named $BPQDs_1$/CN-$rGO_3$, $BPQDs_2$/CN-$rGO_3$, and $BPQDs_3$/CN-$rGO_3$, respectively. The photodegradation efficiencies of the ternary heterojunctions revealed that the photocatalytic activity increased with increasing BPQDs ratio in the photocatalyst


https://doi.org/10.1021/acssuschemeng.3c01055
ACS Sustainable Chem. Eng. 2023, 11, 7560−7572

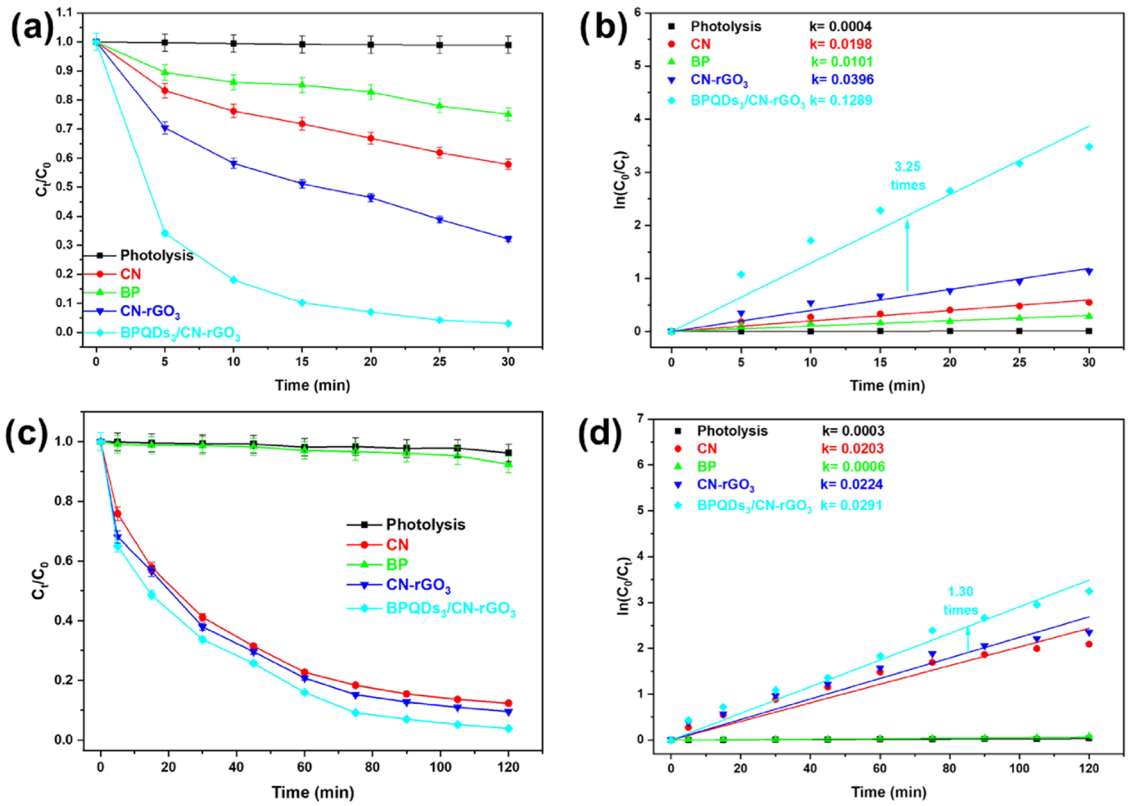



**Figure 4.** (a) Photodegradation of MO under visible light and (b) corresponding first-order plots. (c) Photodegradation of TC under visible light and (d) corresponding first-order plots with CN, BP, CN-rGO, and BPQDs/CN-rGO.

(Figure S9b). The MO degradation efficacy of the BPQDs$_3$/CN-rGO$_3$ heterojunction was 97% in 30 min, which was the best photocatalytic activity that is 3.25 times faster compared to CN-rGO$_3$ (Figure 4a,b). After determining the photocatalyst with the best synergistic effect by combining the structures with different ratios, the other parameters such as organic pollutant concentration and the amount of photocatalyst for the photodegradation of MO were examined in order to understand the scope and limits of the ternary heterojunction (Figure S10). Both the catalyst amount and the reaction time were kept constant likewise the model reaction, and the photodegradation efficiencies were investigated with determined MO concentrations. Compared to 5 ppm, the yields dropped dramatically in the cases of 7.5 and 10 ppm to 65 and 46%, respectively (Figure S10a,b). The performance of the ternary heterojunction was determined to be at 5.0 ppm, and the next step for the optimization was assigned as the amount of the catalyst. When the photodegradation efficiencies were studied with the predetermined 20 and 25 mg amounts of catalysts, the degradation rates were compared with that of 30 mg and they were found to yield 66 and 77%, respectively (Figure S10c,d). As a whole, the optimum photodegradation conditions for the BPQDs$_3$/CN-rGO$_3$ heterojunction were found to be 5.0 ppm MO, 30 mg of photocatalyst, 25 °C, and 30 min, resulting in 97% degradation efficiency of MO with a 0.1289 min$^{-1}$ reaction rate. $^1$H NMR measurements were carried out to detect possible intermediates during the photodegradation of MO (Table S1). The results were obtained by taking the sample from the reaction medium every 5 min, and similar intermediates through the N═N bond cleavage followed by hydroxylation of resulting aromatic intermediates were observed as reported.[46,47]

In lieu of MO, TC was selected as the second organic pollutant to understand further the effectiveness of oxidative species generated by the designed ternary heterojunction, BPQDs$_3$/CN-rGO$_3$ (Figure 4c,d). While the photolysis led to negligibly low photodegradation efficiency, pristine BP was also observed to afford a similar yield after reaching the maximum point at the adsorption−desorption equilibrium (Figure 4c). The ternary heterojunction was found to accelerate the reaction rate and reach the maximum level of photocatalytic activity in TC photodegradation as in MO compared to CN and CN-rGO$_3$. When CN was used alone, the degradation efficiency of 87% increased by 90% with CN-rGO$_3$, while it was observed that rGO in the medium as a conductor facilitated charge separations, and the reaction kinetics increased to 0.0224 min$^{-1}$ (Figure 4c,d). This increase was even higher when BPQDs$_3$/CN-rGO$_3$ was used, resulting in a degradation efficiency of 96% and reaction kinetics of 0.0291 min$^{-1}$. After determining the BPQDs$_3$/CN-rGO$_3$ ternary heterojunction as the best photocatalyst for TC photodegradation, the scope and limits of the catalyst for TC degradation were investigated with other parameters. TC with concentrations of 25 and 75 ppm was degraded under the same conditions (Figure S11a,b). Photodegradation efficiencies were found to be 97% for 25 ppm and 78% for 75 ppm with the rate kinetics of 0.033 and 0.0131 min$^{-1}$, respectively. Therefore, the optimum TC concentration was determined as 25 ppm, and the photodegradation performance of BPQDs$_3$/CN-rGO$_3$ with 25 and 20 mg of photocatalyst was investigated for further studies (Figure S11c,d). When 25 mg of BPQDs$_3$/CN-rGO$_3$ was used, the efficiency was detected at 92% with a rate constant of 0.0240 min$^{-1}$, and 20 mg of catalyst yielded 91% with a rate constant of 0.0236 min$^{-1}$.



https://doi.org/10.1021/acssuschemeng.3c01055
ACS Sustainable Chem. Eng. 2023, 11, 7560−7572

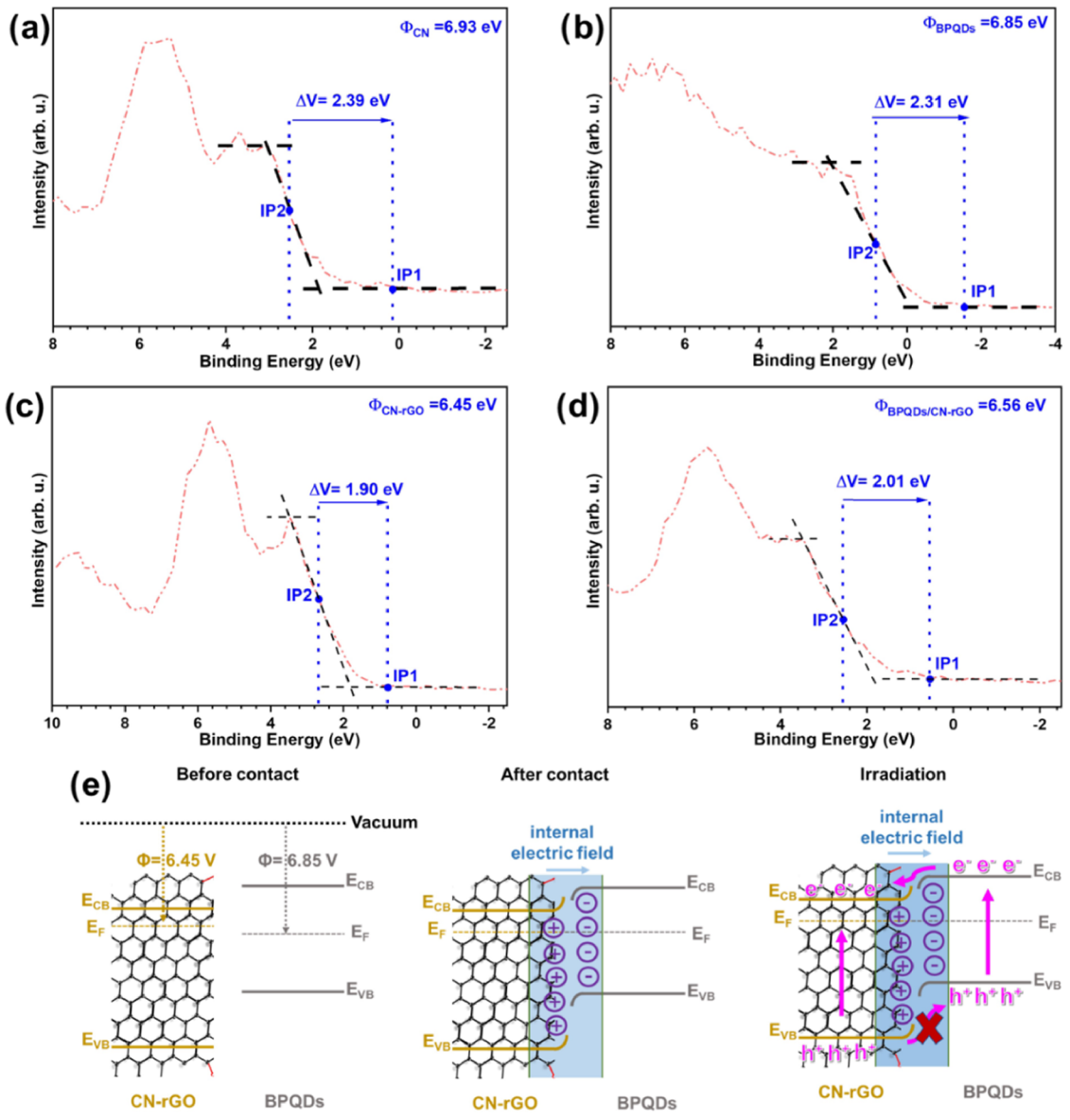


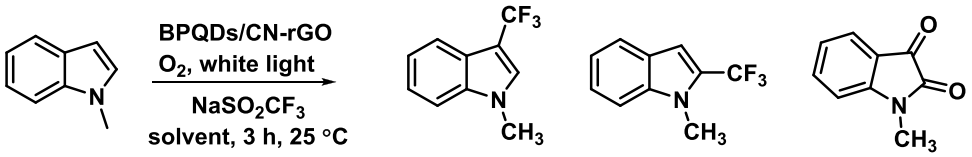

**Figure 5.** Work functions of (a) CN, (b) BPQDs, (c) CN-rGO, and (d) BPQDs/CN-rGO. (e) IEF between semiconductors before, after contact, and under irradiation, resulting in the bending of band edges for CN-rGO and BPQDs.

**Band Alignments and Photooxidation Scope of BPQDs/CN-rGO.** The photocatalytic activity of the constructed ternary structure is related to the band alignments of components in a close manner. To further examine the capacity of BPQDs/CN-rGO, the flat band potentials ($E_f$) of CN and BPQDs were calculated with the help of Mott−Schottky and were calculated as −0.68 and −0.87 V (Ag/AgCl, pH = 7), respectively (Figure S12a,b). The conversion of $E_f$ to normal hydrogen electrode (NHE) potential was achieved according to the well-known equation ($E_{NHE} = E_{(Ag/AgCl)} + 0.197$), and thereby, $E_{NHE}$ values of CN and BPQDs are equal to −0.48 and −0.67 V, respectively.[48] The positive slope of the Mott−Schottky curves in both structures indicates that CN and BPQDs are n-type semiconductors. In previous experimental studies on n-type semiconductors, the conduction band (CB) potential was estimated to be 0.10 V more negative than that of $E_f$, while the $E_f$ value was the same as the Fermi level.[49,50] Based on this information, the CB potential values for BPQDs and CN can be calculated as −0.58 and −0.77 V, respectively. The valence band (VB) potentials of the semiconductors were calculated by using valence band-XPS spectra (Figure S12c,d). The VB potential is the value corresponding to the junction of the tangent and the oblique line near the 0 position of the *X*-axis. The $E_{VB\text{-}XPS}$ for CN and BPQDs were found to be 1.80 and 0.09 eV by examining the intersection in Figure S12c,d, respectively. After that, standard hydrogen electrode potential ($E_{VB\text{-}NHE}$) can be calculated by using the formula of $E_{VB\text{-}NHE} = \Phi + E_{VB\text{-}XPS} - 4.44$, where Φ is the work function of XPS analyzer (4.543 for the device we used).[28,51] Using this formula, the VB values were calculated to be 1.90 and 0.19 V for CN and BPQDs, respectively. By combining the above results, the band energy levels of CN and BPQD semiconductors were depicted as a band diagram, as illustrated in Figure S12e.

In addition to their band potentials, another crucial parameter is their charge transfer direction at the components' interfaces. Analyzing the work functions of binary and ternary structures provides a theoretical base to understand the


https://doi.org/10.1021/acssuschemeng.3c01055
ACS Sustainable Chem. Eng. 2023, 11, 7560−7572

Table 1. Optimization of Trifluoromethylation Using the BPQDs/CN-rGO Photocatalyst[a]




1 2a 2b 2c

| | | | selectivity [%][b] | | |
|---|---|---|---|---|---|
| entry | solvent | conversion [%][b] | 2a | 2b | 2c |
| 1 | $H_2O$, $CH_3NO_2$ | | n.d. | n.d. | trace |
| 2 | MeCN | 11 | trace | trace | trace |
| 3 | DMF | 24 | trace | trace | 15 |
| 4 | DMSO | 70 | 15 | 9 | 7 |
| 5 | DMSO (CN-rGO) | 27 | 14 | 8 | 5 |
| 6 | DMSO (CN) | 16 | 7 | 4 | 4 |

[a]Reaction conditions: 0.1 mmol of **1**, 2.0 equiv. of Langlois reagent (sodium trifluoromethane sulfonate), $O_2$ balloon, and 5 mg of photocatalyst in 1 mL of solvent irradiated by a white light (150 W) for 3 h at 25 °C unless otherwise noted. [b]Conversion and selectivity were calculated based on GC-MS (n.d. stands for not detected).

function of the corresponding band edges and their alignments. Figure 5a–d shows the work function values for CN, BPQDs, CN-rGO, and BPQDs/CN-rGO, which were obtained with the help of VB-XPS spectra. The magnitude of a work function determines the direction of charge flow where materials contact each other at their interfaces. The larger the work function, the further the Fermi level away from the vacuum level of related material, and thus, it is easier to accept an electron from a material that has a relatively small work function. This charge transfer continues until their Fermi levels reach equilibrium and the electron-donating material's surface becomes positively charged and vice versa. The equation of $\Delta V = \Phi - \varphi$ ($\Phi$ is the work function of the material, $\varphi$ is 4.543 eV for the instrument) is used to calculate the corresponding work function of each structure. $\Delta V$ can be found from the relation through the distance of inflection points (**IP1**, change in binding energy at the baseline; **IP2**, the middle point of Fermi energy distribution).[51]

In light of these valuable findings, the work functions of CN, BPQDs, CN-rGO, and BPQDs/CN-rGO were obtained as 6.93, 6.85, 6.45, and 6.56 eV, respectively. The decrease in the work function of CN from 6.93 to 6.45 eV after coupling with rGO indicates that rGO acts as an electron reservoir and the Fermi level of CN gets closer to vacuum (Figure 5c). After the decoration of binary heterojunction with BPQDs, an electron flow is expected to occur from CN-rGO with a higher Fermi level to BPQDs to achieve a balance among them. This flow creates an internal electric field, and the band edges of CN-rGO bend upward while that of BPQDs does a downward bending (Figure 5e). The orientation of the band edges after the contact can be assumed as a suitable direction for electron transfer and migration between these structures. In other words, photogenerated electrons can be expected to migrate from the CB of BPQDs toward the CB of the CN-rGO binary structure in the opposite direction of the internal electric field under light irradiation. Considering the photodegradation process is mostly based on the oxidation ability of a photocatalyst, several experiments were performed to find out whether or not it is a classical type-II heterojunction.

At the outset, to capture the reactive intermediates, $O_2^{\bullet-}$, $^{\bullet}OH$, and $h^+$, 1,4-benzoquinone (BQ), isopropyl alcohol (IPA), and triethanolamine (TEOA) were added to the optimized reaction conditions, respectively (Figure S13). Photogenerated electrons in the CB of both BPQDs and CN-rGO binary heterojunctions are sufficient to generate strongly oxidative $O_2^{\bullet-}$ ($E(O_2/O_2^{\bullet-}) = -0.33$ V vs NHE) species from the dissolved oxygen in the reaction medium. When BQ was used to scavenge $O_2^{\bullet-}$ radicals, a remarkable decrease was observed in the degradation efficiency (15%). When IPA was used to capture the produced $^{\bullet}OH$ radicals in the photocatalytic process, the degradation efficiency was slightly affected and decreased to 91%. TEOA was added to the medium as a sacrificial electron donor, which is known to reduce recombination that can also compete with the pollutant oxidation occurring in the VB. It was observed that the effect of TEOA on MO photodegradation was quite high (degradation efficiency: 19%), as shown in Figure S13. Bearing in mind that the oxidation of TEOA ($E(\text{TEOA/TEOA}^+) = +0.80$ V vs NHE) may only occur in the VB of CN-rGO when the band potentials of structures are considered (Figure S12e),[52] it can be speculated that there is no possible migration of photogenerated holes among the VB of the components in addition to the unfavorable direction of the internal electric field, unlike a classical type-II heterojunction (Figure 5e).

The heterogeneous nature of the obtained ternary heterojunction was investigated for the photodegradation of MO. Up to three cycles, there was no remarkable drop in the degradation efficiency (up to 93%). However, the yield decreased to 89% in the fourth run (Figure S14a). After the recyclability test, the characterization methods such as XRD and TEM were performed. While no change in XRD patterns was detected compared to the original photocatalyst, TEM images revealed slight alterations in the morphology of the ternary heterojunction such as thickening of the edges (Figure S14b,c).

The mechanistic comprehension that underlies the redox ability of the presented catalyst prompted us to apply it to other photooxidation reactions involving the species such as $h^+$ and $O_2^{\bullet-}$.[53] After the introduction of electrophilic trifluoromethyl radical ($^{\bullet}CF_3$) into electron-rich arenes by Langlois' group, many approaches have been investigated for producing high-value molecules containing the Fluor moiety.[54] Albeit the so-called Langlois reagent ($CF_3SO_2Na$) can be used as the source of many species for multipurpose,[55] the formation of



https://doi.org/10.1021/acssuschemeng.3c01055
ACS Sustainable Chem. Eng. 2023, 11, 7560−7572

$^{\bullet}CF_3$ requires single-electron oxidation. Not only to confirm the nonclassical heterojunction type-II of BPQDs/CN-rGO but also to generate the essential $CF_3$-substituted organic molecules, Langlois reagent with high oxidation potential (+1.34 V vs NHE) was chosen.[56] The obtained results are summarized in Table 1. When water was used as it is an optimized solvent in photodegradation, no product was detected (Table 1, **entry 1**).

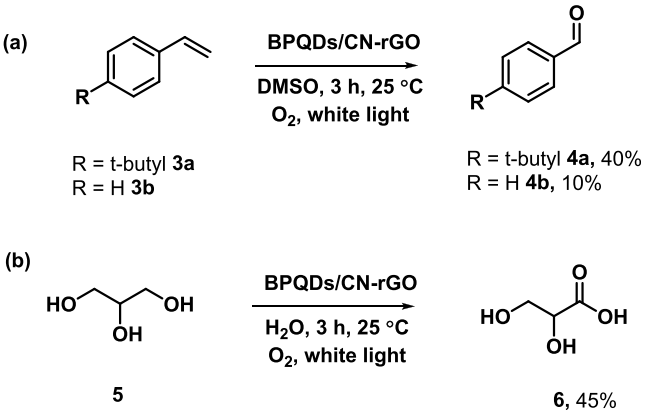
In addition to that, nitromethane yielded almost no product formation while little conversion was observed in the case of MeCN and DMF (Table 1, **entries 1−3**). When DMSO was used as a solvent, the total conversion of **1** was 70% with 24% desired product selectivity (Table 1, **entry 4**). To compare the photocatalytic performance of BPQDs/CN-rGO, the reaction was performed with CN-rGO and CN, and the results showed that the presence of BPQDs has a great impact on this transformation (Table 1, **entries 5,6**). The obtained product formation further confirmed the oxidation of Langlois reagent by the VB of BPQDs/CN-rGO and there was no migration among the semiconducting materials (Figure 5e). As depicted in Table S3, compared to common homogeneous photocatalysts and metal-based catalysts, the field of trifluoromethylation of heteroarenes using Langlois reagent has been expanded with metal-free BPQDs/CN-rGO heterojunction, which is also the first example of a metal-free BPQD-based photocatalyst for photoredox organic transformation.

In addition, the yielded products prompted us to investigate even more the utilization of generated ROS by the photocatalyst. The addition of $-SO_2Me$ to **1** was also detected as expected since DMSO is known to react as a reagent with in situ-generated ROS (Scheme S2).[57,58] The formation of C=C bond cleavage was also observed, leading to product **2e**. Both products gave us a clue about the formation of singlet oxygen ($^1O_2$) (another possible ROS, OH was excluded via IPA in scavenger experiments (Figure S13)) since it may oxidize DMSO to generate $^{\bullet}SO_2Me$[59] while product **2e** is the result of 2 + 2 cycloaddition[60] reaction with $^1O_2$ (Scheme S2). We next turned our attention to another transformation with the knowledge that there is a known cooperation of $^1O_2$ and $O_2^{\bullet-}$ to cleave double bonds to aldehydes.[61,62] 4-*tert*-Butyl styrene (**3a**) was selected as a model substrate and it was successfully converted to the related benzaldehyde (**4a**) in 40% yield selectively (Scheme 1a). Also, the double bonds of styrene (**3b**) were activated with the generated $^1O_2$ despite being somewhat less effective (10%) (Scheme 1a).

With the confidence of having $O_2^{\bullet-}$, h+, and $^1O_2$ as active agents,[63] oxidation of glycerol was performed owing to its multifunctional structure having a vital role in the biodiesel industry.[64,65] Therefore, it is important to produce one of these valuable products selectively (Scheme S3). Water was chosen as the reaction medium and the effect of ROS generation in aqueous media for the oxidation process of glycerol was monitored. When the reaction was carried out under base-free conditions, there was no conversion and glycerol remained intact. The addition of NaOH to the reaction medium favored the photooxidation of glycerol with BPQDs/CN-rGO, and glyceric acid was formed in 45% yield (Scheme 1b). All of these aforementioned photooxidation reactions clearly showed the scope therewith the chemical stability of ternary heterojunction toward highly active ROS and harsh conditions (NaOH, $^{\bullet}CF_3$).

To bring all of the photocatalytic experiments together, a plausible mechanism of nonclassical-type-II heterojunction is

**Scheme 1. (a) C=C Bond Cleavage of Styrene Derivatives, (b) Photooxidation of Glycerol**




illustrated in Figure 6. First, after photogenerated electron flow from the CB of BPQDs toward that of CN-rGO under light

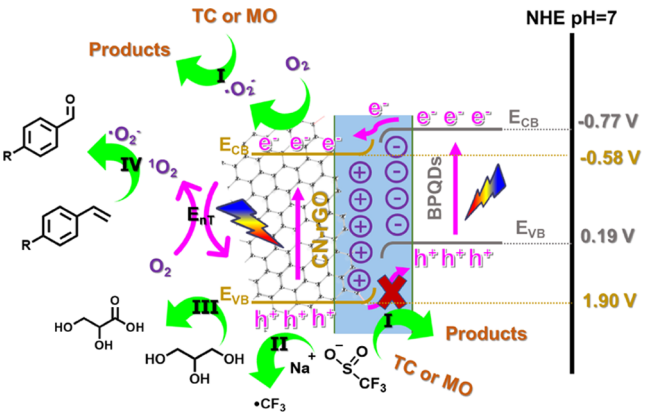



**Figure 6.** Plausible reaction mechanism for the studied photoredox reactions.

irradiation, molecular oxygen is reduced by the CB of the heterojunction to form $O_2^{\bullet-}$ species (**I**). In addition to that, $^1O_2$ species are generated via energy transfer ($E_{nT}$) from the BPQDs/CN-rGO heterojunction. Both these species are involved in the photodegradation of organic pollutants (**I**) and C=C bond cleavage of styrene (**IV**). In parallel to this, the photogenerated holes take place in the oxidation of organic pollutants (**I**), Langlois reagent (**II**), and glycerol (**III**) owing to the ability of high charge separation in the designed ternary heterojunction.

## CONCLUSIONS

As a result, we have introduced the photocatalytic ability of BPQDs/CN-rGO in various organic transformations proceeding with a photooxidation mechanism. BPQDs/CN-rGO as a metal-free photocatalyst was synthesized via the UALE method and characterized with advanced techniques. The contents of the individual components to construct binary and ternary heterojunctions were optimized based on the photodegradation of MO and TC finding out the synergistic interaction among them. The superior photocatalytic performance of the ternary heterojunction was obtained for MO (30 min, 5 ppm) and TC (120 min, 25 ppm) with 0.1289 and 0.0335 $min^{-1}$ reaction kinetics, respectively. The redox capacity that


https://doi.org/10.1021/acssuschemeng.3c01055
ACS Sustainable Chem. Eng. 2023, 11, 7560−7572

underlies the photocatalyst with the best photoredox performance was enlightened by measuring the Fermi levels experimentally. Not only confirming the nonclassical-type-II heterojunction of BPQDs/CN-rGO but also extending its applicability, various organic transformations occurring with the presence of $O_2^{\bullet-}$, h+, and $^1O_2$ were performed. These essential species enabled the oxidation of glycerol selectively to glyceric acid (45%) and styrene to benzaldehyde derivatives (40%) whereas highly challenging Langlois reagent to $^{\bullet}CF_3$ radicals proving the active role of $h^+$. We expect this ternary heterojunction, BPQDs/CN-rGO, to be of broad utility in different conditions for many other applications.

## ■ ASSOCIATED CONTENT

### Supporting Information

The Supporting Information is available free of charge at https://pubs.acs.org/doi/10.1021/acssuschemeng.3c01055.

Characterization of catalysts (XRD, XPS, FTIR, Raman, band alignment calculations (Mott−Schottky plots and XPS-VB), postcharacterization), synthesis of materials (general procedures), and products (NMR, GC-MS) (PDF)

## ■ AUTHOR INFORMATION


### Corresponding Author

**Onder Metin** − *Department of Chemistry, College of Sciences, Koç University, 34450 Istanbul, Türkiye; Koç University Surface Science and Technology Center (KUYTAM), 34450 Istanbul, Türkiye; Koç University Tüpraş Energy Center (KUTEM), 34450 Istanbul, Türkiye;* orcid.org/0000-0003-1622-4992; Email: ometin@ku.edu.tr

### Authors

**Zafer Eroglu** − *Department of Chemistry, College of Sciences, Koç University, 34450 Istanbul, Türkiye; Division of Nanoscience and Nanoengineering, Institute of Natural and Applied Sciences, Atatürk University, 25240 Erzurum, Türkiye;* orcid.org/0000-0002-0601-2526

**Melek Sermin Ozer** − *Department of Chemistry, College of Sciences, Koç University, 34450 Istanbul, Türkiye;* orcid.org/0000-0003-4840-8542

Complete contact information is available at: https://pubs.acs.org/10.1021/acssuschemeng.3c01055


### Author Contributions

Z.E.: Conceptualization, formal analysis, methodology, validation, investigation, writing—original draft, and visualization. M.S.O.: Conceptualization, formal analysis, methodology, validation, investigation, writing—original draft, visualization, and project administration. O.M.: Conceptualization, writing—review and editing, supervision, funding acquisition, project administration, validation, and provision.

### Notes

The authors declare no competing financial interest.

## ■ ACKNOWLEDGMENTS

This work is a chapter in the Ph.D. thesis of Z.E. Ö.M. thanks the Turkish Academy of Sciences (TÜBA) for the financial support. The authors thank Temirlan Kubanaliev for his support. Z.E. thanks the Council of Higher Education (YOK) and the Scientific and Technological Research Council of Turkey (TÜBİTAK) for the Ph.D. scholarship (YOK/100−2000 and TÜBITAK 2211-C).

## ■ REFERENCES


(1) Herrmann, J.-M. Photocatalysis. In *Kirk-Othmer Encyclopedia of Chemical Technology*; John Wiley & Sons, Inc.: Hoboken, NJ, USA, 2017; pp 1−44.

(2) Ameta, R.; Solanki, M. S.; Benjamin, S.; Ameta, S. C. Photocatalysis. In *Advanced Oxidation Processes for Waste Water Treatment*; Elsevier, 2018; pp 135−175.

(3) Wang, H.; Li, X.; Zhao, X.; Li, C.; Song, X.; Zhang, P.; Huo, P.; Li, X. A Review on Heterogeneous Photocatalysis for Environmental Remediation: From Semiconductors to Modification Strategies. *Chin. J. Catal.* **2022**, *43*, 178−214.

(4) Xu, J.; Wu, H.-T.; Wang, X.; Xue, B.; Li, Y.-X.; Cao, Y. A New and Environmentally Benign Precursor for the Synthesis of Mesoporous g-$C_3N_4$ with Tunable Surface Area. *Phys. Chem. Chem. Phys.* **2013**, *15*, 4510−4517.

(5) Wang, X.; Maeda, K.; Thomas, A.; Takanabe, K.; Xin, G.; Carlsson, J. M.; Domen, K.; Antonietti, M. A Metal-Free Polymeric Photocatalyst for Hydrogen Production from Water under Visible Light. *Nat. Mater.* **2008**, *8*, 76−80.

(6) Lee, Y.; Kwon, M. S. Emerging Organic Photoredox Catalysts for Organic Transformations. *Eur. J. Org. Chem.* **2020**, *2020*, 6028−6043.

(7) Kisch, H. Semiconductor Photocatalysis–Mechanistic and Synthetic Aspects. *Angew. Chem., Int. Ed.* **2013**, *52*, 812−847.

(8) Mills, A.; Le Hunte, S. An Overview of Semiconductor Photocatalysis. *J. Photochem. Photobiol., A* **1997**, *108*, 1−35.

(9) Zhu, D.; Zhou, Q. Action and Mechanism of Semiconductor Photocatalysis on Degradation of Organic Pollutants in Water Treatment: A Review. *Environ. Nanotechnol., Monit. Manage.* **2019**, *12*, No. 100255.

(10) Su, Q.; Li, Y.; Hu, R.; Song, F.; Liu, S.; Guo, C.; Zhu, S.; Liu, W.; Pan, J. Heterojunction Photocatalysts Based on 2D Materials: The Role of Configuration. *Adv. Sustainable Syst.* **2020**, *4*, No. 2000130.

(11) Cao, S.; Low, J.; Yu, J.; Jaroniec, M. Polymeric Photocatalysts Based on Graphitic Carbon Nitride. *Adv. Mater.* **2015**, *27*, 2150−2176.

(12) Li, W.; Wang, Z.; Li, Y.; Ghasemi, J. B.; Li, J.; Zhang, G. Visible-NIR Light-Responsive 0D/2D CQDs/$Sb_2WO_6$ Nanosheets with Enhanced Photocatalytic Degradation Performance of RhB: Unveiling the Dual Roles of CQDs and Mechanism Study. *J. Hazard. Mater.* **2022**, *424*, No. 127595.

(13) Wang, Z.; Cheng, Q.; Wang, X.; Li, J.; Li, W.; Li, Y.; Zhang, G. Carbon Dots Modified Bismuth Antimonate for Broad Spectrum Photocatalytic Degradation of Organic Pollutants: Boosted Charge Separation, DFT Calculations and Mechanism Unveiling. *Chem. Eng. J.* **2021**, *418*, No. 129460.

(14) Wang, X.; Ren, Y.; Li, Y.; Zhang, G. Fabrication of 1D/2D $BiPO_4$/g-$C_3N_4$ Heterostructured Photocatalyst with Enhanced Photocatalytic Efficiency for NO Removal. *Chemosphere* **2022**, *287*, No. 132098.

(15) Wang, Y.; Wang, K.; Wang, J.; Wu, X.; Zhang, G. $Sb_2WO_6$/BiOBr 2D Nanocomposite S-Scheme Photocatalyst for NO Removal. *J. Mater. Sci. Technol.* **2020**, *56*, 236−243.

(16) Xu, Q.; Zhang, L.; Cheng, B.; Fan, J.; Yu, J. S-Scheme Heterojunction Photocatalyst. *Chem* **2020**, *6*, 1543−1559.

(17) Zhang, L.; Gao, L.-F.; Li, L.; Hu, C.-X.; Yang, Q.-Q.; Zhu, Z.-Y.; Peng, R.; Wang, Q.; Peng, Y.; Jin, J.; Zhang, H.-L. Negatively Charged 2D Black Phosphorus for Highly Efficient Covalent Functionalization. *Mater. Chem. Front.* **2018**, *2*, 1700−1706.

(18) Long, L.; Niu, X.; Yan, K.; Zhou, G.; Wang, J.; Wu, X.; Chu, P. K. Highly Fluorescent and Stable Black Phosphorus Quantum Dots in Water. *Small* **2018**, *14*, No. 1803132.

(19) Yuan, Y. J.; Yang, S.; Wang, P.; Yang, Y.; Li, Z.; Chen, D.; Yu, Z. T.; Zou, Z.-G. Bandgap-Tunable Black Phosphorus Quantum Dots: Visible-Light-Active Photocatalysts. *Chem. Commun.* **2018**, *54*, 960−963.

(20) Lei, W.; Pang, X.; Ge, G.; Liu, G. Recent Progress on Black Phosphorus Quantum Dots for Full-Spectrum Solar-to-Chemical Energy Conversion. *Nano Today* **2021**, *39*, No. 101183.
(21) Zhang, X.; Xie, H.; Liu, Z.; Tan, C.; Luo, Z.; Li, H.; Lin, J.; Sun, L.; Chen, W.; Xu, Z.; Xie, L.; Huang, W.; Zhang, H. Black Phosphorus Quantum Dots. *Angew. Chem., Int. Ed.* **2015**, *54*, 3653−3657.
(22) Xiang, Q.; Yu, J.; Jaroniec, M. Enhanced Photocatalytic H2-Production Activity of Graphene-Modified Titania Nanosheets. *Nanoscale* **2011**, *3*, 3670−3678.
(23) Behura, S. K.; Wang, C.; Wen, Y.; Berry, V. Graphene−Semiconductor Heterojunction Sheds Light on Emerging Photovoltaics. *Nat. Photonics* **2019**, *13*, 312−318.
(24) Yalın, A. S.; Sündü, B.; Özer, M. S.; Mekkaoui, A. A.; El Houssame, S.; Metin, Ö. Catalytic Dehydrogenation of Natural Terpenes via CuPd Alloy Nanoparticles Generated on Mesoporous Graphitic Carbon Nitride. *Appl. Organomet. Chem.* **2023**, *37*, No. e6943.
(25) Yanalak, G.; Yılmaz, S.; Eroglu, Z.; Aslan, E.; Metin, O.; Patir, I. H. Transition Metal (Ni, Co)-Doped Graphitic Carbon Nitride/$MoS_2$ Heterojunctions as Efficient Photocatalysts for Hydrogen Evolution Reaction under Visible Light. *Int. J. Energy Res.* **2022**, *46*, 17189−17203.
(26) Huang, D.; Wang, G.; Cheng, M.; Zhang, G.; Chen, S.; Liu, Y.; Li, Z.; Xue, W.; Lei, L.; Xiao, R. Optimal Preparation of Catalytic Metal-Organic Framework Derivatives and Their Efficient Application in Advanced Oxidation Processes. *Chem. Eng. J.* **2021**, *421*, No. 127817.
(27) Chen, S.; Huang, D.; Du, L.; Lei, L.; Chen, Y.; Wang, G.; Wang, Z.; Zhou, W.; Tao, J.; Li, R.; Zhou, C. Peroxymonosulfate Activation by Surface-Modified Bismuth Vanadate for Ciprofloxacin Abatement under Visible Light: Insights into the Generation of Singlet Oxygen. *Chem. Eng. J.* **2022**, *444*, No. 136373.
(28) Xiong, J.; Li, X.; Huang, J.; Gao, X.; Chen, Z.; Liu, J.; Li, H.; Kang, B.; Yao, W.; Zhu, Y. CN/rGO@BPQDs High-Low Junctions with Stretching Spatial Charge Separation Ability for Photocatalytic Degradation and $H_2O_2$ Production. *Appl. Catal., B* **2020**, *266*, No. 118602.
(29) Tiouitchi, G.; Ali, M. A.; Benyoussef, A.; Hamedoun, M.; Lachgar, A.; Benaissa, M.; Kara, A.; Ennaoui, A.; Mahmoud, A.; Boschini, F.; Oughaddou, H.; El Kenz, A.; Mounkachi, O. An Easy Route to Synthesize High-Quality Black Phosphorus from Amorphous Red Phosphorus. *Mater. Lett.* **2019**, *236*, 56−59.
(30) Eroglu, Z.; Ozer, M. S.; Kubanaliev, T.; Kilic, H.; Metin, Ö. Synergism between Few-Layer Black Phosphorus and Graphitic Carbon Nitride Enhances the Photoredox C-H Arylation under Visible Light Irradiation. *Catal. Sci. Technol.* **2022**, *12*, 5379−5389.
(31) Kocaarslan, A.; Eroglu, Z.; Yilmaz, G.; Metin, O.; Yagci, Y. Expanding the Scope of 2D Black Phosphorus Catalysis to the Near-Infrared Light Initiated Free Radical Photopolymerization. *ACS Macro Lett.* **2021**, *10*, 679−683.
(32) Song, X.; Hu, Y.; Zheng, M.; Wei, C. Solvent-Free in Situ Synthesis of g-$C_3N_4$/{001}$TiO_2$ Composite with Enhanced UV- and Visible-Light Photocatalytic Activity for NO Oxidation. *Appl. Catal., B* **2016**, *182*, 587−597.
(33) Dağalan, Z.; Behboudikhiavi, S.; Turgut, M.; Sevim, M.; Kasapoğlu, A. E.; Nişanci, B.; Metin, Ö. Nickel-Palladium Alloy Nanoparticles Supported on Reduced Graphene Oxide Decorated with Metallic Aluminum Nanoparticles (Al-rGO/NiPd): A Multifunctional Catalyst for the Transfer Hydrogenation of Nitroarenes and Olefins Using Water as a Hydrogen Source. *Inorg. Chem. Front.* **2021**, *8*, 2200−2212.
(34) Hummers, W. S.; Offeman, R. E. Preparation of Graphitic Oxide. *J. Am. Chem. Soc.* **1958**, *80*, No. 1339.
(35) Yanalak, G.; Doganay, F.; Eroglu, Z.; Kucukkececi, H.; Aslan, E.; Ozmen, M.; Bas, S. Z.; Metin, O.; Patir, I. H. Ternary Nanocomposites of Mesoporous Graphitic Carbon Nitride/Black Phosphorus/Gold Nanoparticles (mpg-CN/BP-Au) for Photocatalytic Hydrogen Evolution and Electrochemical Sensing of Paracetamol. *Appl. Surf. Sci.* **2021**, *557*, No. 149755.
(36) Sun, Z.; Xie, H.; Tang, S.; Yu, X. F.; Guo, Z.; Shao, J.; Zhang, H.; Huang, H.; Wang, H.; Chu, P. K. Ultrasmall Black Phosphorus Quantum Dots: Synthesis and Use as Photothermal Agents. *Angew. Chem., Int. Ed.* **2015**, *54*, 11526−11530.
(37) Cai, X.; Liu, H.; Zhi, L.; Wen, H.; Yu, A.; Li, L.; Chen, F.; Wang, B. A g-$C_3N_4$/rGO Nanocomposite as a Highly Efficient Metal-Free Photocatalyst for Direct C−H Arylation under Visible Light Irradiation. *RSC Adv.* **2017**, *7*, 46132−46138.
(38) Zheng, Y.; Chen, Y.; Gao, B.; Lin, B.; Wang, X. Phosphorene-Based Heterostructured Photocatalysts. *Engineering* **2021**, *7*, 991−1001.
(39) Pahari, S. K.; Doong, R.-A. Few-Layered Phosphorene−Graphitic Carbon Nitride Nanoheterostructure as a Metal-Free Photocatalyst for Aerobic Oxidation of Benzyl Alcohol and Toluene. *ACS Sustainable Chem. Eng.* **2020**, *8*, 13342−13351.
(40) Park, J.-E.; Oh, N.; Nam, H.; Park, J.-H.; Kim, S.; Jeon, J. S.; Yang, M. Efficient Capture and Raman Analysis of Circulating Tumor Cells by Nano-Undulated AgNPs-rGO Composite SERS Substrates. *Sensors* **2020**, *20*, No. 5089.
(41) Han, S. T.; Hu, L.; Wang, X.; Zhou, Y.; Zeng, Y. J.; Ruan, S.; Pan, C.; Peng, Z. Black Phosphorus Quantum Dots with Tunable Memory Properties and Multilevel Resistive Switching Characteristics. *Adv. Sci.* **2017**, *4*, No. 1600435.
(42) Makuła, P.; Pacia, M.; Macyk, W. How to Correctly Determine the Band Gap Energy of Modified Semiconductor Photocatalysts Based on UV-Vis Spectra. *J. Phys. Chem. Lett.* **2018**, *9*, 6814−6817.
(43) Landi, S.; Segundo, I. R.; Freitas, E.; Vasilevskiy, M.; Carneiro, J.; Tavares, C. J. Use and Misuse of the Kubelka-Munk Function to Obtain the Band Gap Energy from Diffuse Reflectance Measurements. *Solid State Commun.* **2022**, *341*, No. 114573.
(44) Li, Q.; Anpo, M.; Wang, X. Application of Photoluminescence Spectroscopy to Elucidate Photocatalytic Reactions at the Molecular Level. *Res. Chem. Intermed.* **2020**, *46*, 4325−4344.
(45) Wang, G.; Huang, D.; Cheng, M.; Chen, S.; Zhang, G.; Du, L.; Lei, L.; Chen, Y.; Li, R.; Liu, Y. An Insight into the Bridging Role of $Co_3O_4$ in MOF-Derived Binary Metal Oxide Modified Sheet-like g-$C_3N_4$ for Photo-Assisted Peroxymonosulfate Activation. *Environ. Sci. Nano* **2022**, *9*, 4393−4410.
(46) Shan, R.; Lu, L.; Gu, J.; Zhang, Y.; Yuan, H.; Chen, Y.; Luo, B. Photocatalytic Degradation of Methyl Orange by Ag/$TiO_2$/Biochar Composite Catalysts in Aqueous Solutions. *Mater. Sci. Semicond. Process.* **2020**, *114*, No. 105088.
(47) Leuterio, J. C.; Camacho, D. H.; Bantang, J. P. O.; Argamino, C. R. A. Influence of Precursor Chemistry in the Property of Carbon Nanodots and Its Application for the Degradation of Methyl Orange. *Mater. Chem. Phys.* **2022**, *278*, No. 125668.
(48) Ozer, M. S.; Eroglu, Z.; Yalin, A. S.; Kılıç, M.; Rothlisberger, U.; Metin, O. Bismuthene as a Versatile Photocatalyst Operating under Variable Conditions for the Photoredox C−H Bond Functionalization. *Appl. Catal., B* **2022**, *304*, No. 120957.
(49) Yang, Q. Q.; Liu, R. T.; Huang, C.; Huang, Y. F.; Gao, L. F.; Sun, B.; Huang, Z. P.; Zhang, L.; Hu, C. X.; Zhang, Z. Q.; Sun, C. L.; Wang, Q.; Tang, Y. L.; Zhang, H. L. 2D Bismuthene Fabricated: Via Acid-Intercalated Exfoliation Showing Strong Nonlinear near-Infrared Responses for Mode-Locking Lasers. *Nanoscale* **2018**, *10*, 21106−21115.
(50) Zhang, T.; Yu, J.; Huang, J.; Lan, S.; Lou, Y.; Chen, J. MoC/$MAPbI_3$hybrid Composites for Efficient Photocatalytic Hydrogen Evolution. *Dalton Trans.* **2021**, *50*, 10860−10866.
(51) Li, X.; Luo, Q.; Han, L.; Deng, F.; Yang, Y.; Dong, F. Enhanced Photocatalytic Degradation and $H_2$ Evolution Performance of N−CDs/S-$C_3N_4$ S-Scheme Heterojunction Constructed by $\pi$-$\pi$ Conjugate Self-Assembly. *J. Mater. Sci. Technol.* **2022**, *114*, 222−232.
(52) Pellegrin, Y.; Odobel, F. Sacrificial Electron Donor Reagents for Solar Fuel Production. *C. R. Chim.* **2017**, *20*, 283−295.
(53) Xu, C.; Pan, Y.; Wan, G.; Liu, H.; Wang, L.; Zhou, H.; Yu, S. H.; Jiang, H. L. Turning on Visible-Light Photocatalytic C-H Oxidation over Metal-Organic Frameworks by Introducing Metal-


https://doi.org/10.1021/acssuschemeng.3c01055
ACS Sustainable Chem. Eng. 2023, 11, 7560−7572

to-Cluster Charge Transfer. *J. Am. Chem. Soc.* **2019**, *141*, 19110−19117.
(54) Langlois, B. R.; Billard, T.; Mulatier, J. C.; Yezeguelian, C. A New Preparation of Trifluoromethanesulfinate Salts. *J. Fluorine Chem.* **2007**, *128*, 851−856.
(55) Kaboudin, B.; Ghashghaee, M.; Bigdeli, A.; Farkhondeh, A.; Eskandari, M.; Esfandiari, H. Recent Advances on the Application of Langlois' Reagent in Organic Transformations. *ChemistrySelect* **2021**, *6*, 12998−13014.
(56) Ghosh, I.; Khamrai, J.; Savateev, A.; Shlapakov, N.; Antonietti, M.; König, B. Organic Semiconductor Photocatalyst Can Bifunctionalize Arenes and Heteroarenes. *Science* **2019**, *365*, 360−366.
(57) Hyland, K.; Auclair, C. The Formation of Superoxide Radical Anions by a Reaction between $O_2$, OH- and Dimethyl Sulfoxide. *Biochem. Biophys. Res. Commun.* **1981**, *102*, 531−537.
(58) Wu, X.-F.; Natte, K. The Applications of Dimethyl Sulfoxide as Reagent in Organic Synthesis. *Adv. Synth. Catal.* **2016**, *358*, 336−352.
(59) Lutkus, L. V.; Rickenbach, S. S.; McCormick, T. M. Singlet Oxygen Quantum Yields Determined by Oxygen Consumption. *J. Photochem. Photobiol., A* **2019**, *378*, 131−135.
(60) Zhang, C.; Li, S.; Bureš, F.; Lee, R.; Ye, X.; Jiang, Z. Visible Light Photocatalytic Aerobic Oxygenation of Indoles and PH as a Chemoselective Switch. *ACS Catal.* **2016**, *6*, 6853−6860.
(61) Li, J.; Zhao, J.; Ma, C.; Yu, Z.; Zhu, H.; Yun, L.; Meng, Q. Visible-Light-Driven Oxidative Cleavage of Alkenes Using Water-Soluble CdSe Quantum Dots. *ChemSusChem* **2021**, *14*, 4985−4992.
(62) Wang, H.; Jia, R.; Hong, M.; Miao, H.; Ni, B.; Niu, T. Hydroxyl Radical-Mediated Oxidative Cleavage of CC Bonds and Further Esterification Reaction by Heterogeneous Semiconductor Photocatalysis. *Green Chem.* **2021**, *23*, 6591−6597.
(63) Guo, L.; Sun, Q.; Marcus, K.; Hao, Y.; Deng, J.; Bi, K.; Yang, Y. Photocatalytic Glycerol Oxidation on $Au_xCu$-CuS@$TiO_2$ Plasmonic Heterostructures. *J. Mater. Chem. A* **2018**, *6*, 22005−22012.
(64) Fan, L.; Liu, B.; Liu, X.; Senthilkumar, N.; Wang, G.; Wen, Z. Recent Progress in Electrocatalytic Glycerol Oxidation. *Energy Technol.* **2021**, *9*, No. 2000804.
(65) Yang, L.; Li, X.; Chen, P.; Hou, Z. Selective Oxidation of Glycerol in a Base-Free Aqueous Solution: A Short Review. *Chin. J. Catal.* **2019**, *40*, 1020−1034.


https://doi.org/10.1021/acssuschemeng.3c01055
*ACS Sustainable Chem. Eng.* 2023, 11, 7560−7572